Tiittanen, T.; Karppinen, M.

Structure evolution upon chemical and physical pressure in (Sr1−xBax)2FeSbO6

Published in:
Journal of Solid State Chemistry

DOI:
10.1016/j.jssc.2016.11.033

Published: 01/02/2017

Document Version
Peer reviewed version

Structure evolution upon chemical and physical pressure in $(Sr_{1-x}Ba_x)_2FeSbO_6$

T. Tiittanen and M. Karppinen*

Department of Chemistry, Aalto University, FI-00076 Espoo, Finland

*maarit.karppinen@aalto.fi

Abstract

Here we demonstrate the gradual structural transformation from the monoclinic *I*2/*m* to tetragonal *I*4/*m*, cubic *Fm*-3*m* and hexagonal $P6_3/mmc$ structure upon the isovalent larger-for-smaller A-site cation substitution in the B-site ordered double-perovskite system $(Sr_{1-x}Ba_x)_2FeSbO_6$. This is the same transformation sequence previously observed up to *Fm*-3*m* upon heating the parent Sr_2FeSbO_6 phase to high temperatures. High-pressure treatment, on the other hand, transforms the hexagonal $P6_3/mmc$ structure of the other end member Ba_2FeSbO_6 back to the cubic *Fm*-3*m* structure. Hence we may conclude that chemical pressure, physical pressure and decreasing temperature all work towards the same direction in the $(Sr_{1-x}Ba_x)_2FeSbO_6$ system. Also shown is that with increasing Ba-for-Sr substitution level, i.e. with decreasing chemical pressure effect, the degree-of-order among the B-site cations, Fe and Sb, decreases.

Keywords: high-pressure synthesis, chemical pressure, double perovskite, crystal structure, cation order

1. Introduction

Perovskite-type oxides derived from the general ABO_3 formula possess a wide variety of both scientifically and commercially interesting properties depending on the choice of the constituting elements. The stability of the perovskite structure for the different A and B constituents is commonly discussed in terms of the Goldschmidt's tolerance factor (t) [1]

$$t = \frac{r_A + r_O}{\sqrt{2}(r_B + r_O)} \quad (1)$$

where r_A, r_B and r_O are the ionic radii of the respective ions calculated from Shannon's ionic radii [2]; ideal cubic perovskites then usually fall between the values 0.95–1.0. There are also multiple hexagonal non-perovskite phases known with the same ABO_3 stoichiometry and $t > 1$ [3,4]. At the same time, perovskites with t lower than unity may have pseudocubic symmetries such as tetragonal or — like the mineral perovskite $CaTiO_3$ — orthorhombic, which then often transform into cubic phases at higher temperatures [5–8]. This symmetry-change trend can also be reversed (i) by cooling, (ii) through smaller-for-larger cation substitution, or (iii) by applying pressure [5]. In particular, the high-pressure treatment is an effective method for synthesizing novel perovskites and related complex oxides which are unreachable under conventional solid state synthesis conditions [9–12].

The perovskite structure can be viewed as a three-dimensional framework of corner-sharing octahedra formed by the B-site cations with surrounding six oxygen anions, the A-site cations then lying in the voids of the grid. The unit cell of the structure depends on the space group chosen. Usually the non-standard setting of a space group is chosen to give the "A-site centred" view of the structure. The crystallographic diversity of perovskites can be thought to originate from the tilting of the BO_6 octahedra. The chemical diversity is due to the flexibility of both the A and B cation sites to accommodate a large number of different cations. When the cation site is simultaneously co-occupied by two different metal species, the long-range ordering of the different cations is possible, at the A or the B site, or even at the both sites simultaneously; also different ordering patterns are known. For the ordered arrangement not only the symmetry but also the size of the unit cell changes. The current work concerns so-called B-site ordered double perovskites, $A_2B'B''O_6$, where the ratio of the two B-site cation species is 1:1 [4]. These double perovskites have been highlighted in recent years for a variety of exciting functional properties such as the tunnelling magnetoresistance in the room-temperature half-metal Sr_2FeMoO_6 for e.g. magnetic memory applications [13] and the mixed oxide-ion and electronic conductivity in Sr_2MgMoO_6 for solid oxide fuel cell anodes [14,15].

The most common pattern of ordering for the $A_2B'B''O_6$ compounds is the rock-salt-type three-dimensional ordering in which each B' cation is surrounded by six B'' cations, and vice versa. Another type but much rarer is the layered ordering, in which the layers are formed by the $B'O_6$ and $B''O_6$ octahedra and the ordering is therefore one dimensional. Also a few cases are known for which the ordering occurs in columns and the ordering propagation is two dimensional [4,14]. Ordering is not always complete but may also be only partial; the degree-of-order is expressed with the Bragg-Williams long-range order parameter (S), defined as

$$S = 2g - 1 \quad (2)$$

where g is the proportional occupancy of the ion at its primary crystallographic site. In completely disordered structures there is only one B site which is randomly occupied by the B' and B'' cations, such that $g = 0.5$ and $S = 0$. In fully ordered samples both B' and B'' cations occupy their own primary, crystallographically unique sites without so-called anti-site defects; accordingly $g = 1$ and $S = 1$. Then in partially ordered samples there is certain anti-site occupancy. Another type of disordering seen for the $A_2B'B''O_6$ double perovskites is the presence of anti-phase boundaries [17]. Usually ordering of the B-site cations in the double perovskites is a desirable feature, since it for example enables interesting and useful physical phenomena through the interplay between the cations [16,18–22].

Factors affecting the ordering include the oxidation states and ionic radii of the cations, Jahn-Teller distortion as well as the magnetic, electronic and bonding properties of the cations. The difference between the charges of the two B-site cations is probably the most influential factor: the larger the difference is, the higher is the equilibrium degree-of-order at the B-site. As a rule of thumb, if the charge difference between the B' and B'' cations is larger than two, complete ordering is commonly achieved. For the particular case of the $A^{II}_2B^{III}B^{V}O_6$ composition various S values are typically observed depending on the synthesis conditions [23]. Thermodynamically samples with the highest degree-of-order are obtained using low synthesis temperatures. However, at low temperatures cation diffusion is slow and the degree-of-order may become kinetically controlled [24]. Thus, in practice to obtain highly ordered $A^{II}_2B^{III}B^{V}O_6$ samples, elongated synthesis periods at moderate temperatures are required. The actual degree-of-order depends also on the particular A, B' and B'' cations; empirically, it seems that for a certain B'-B'' combination S increases with decreasing A cation radius [23,25].

We have chosen the $(Sr_{1-x}Ba_x)_2FeSbO_6$ system as an interesting model system to study the effects of chemical pressure through isovalent A-site cation substitution and physical pressure through a high-pressure (HP) heat treatment on the cation ordering and crystal symmetry. The parent Sr_2FeSbO_6 phase is an ordered pseudocubic perovskite [6] while the other end-member of the series, Ba_2FeSbO_6, has a hexagonal non-ordered non-perovskite structure [3,26]. At room temperature (RT), Sr_2FeSbO_6 was initially believed to possess a monoclinic structure with space group $P2_1/n$ [3,26] but recent studies showed that the space group is actually monoclinic $I2/m$ [6]. However, synthesis conditions may have significant effect on the crystal symmetry as seen e.g. in the cases of Ba_2FeSbO_6 and $BaFeO_3$ [27,28]. Upon heating, Sr_2FeSbO_6 transforms to tetragonal $I4/m$ at 673-703 °C and finally to cubic $Fm\text{-}3m$ at 773 °C [6]. Then upon cooling down to low temperatures the structure of Sr_2FeSbO_6 transforms to $P2_1/n$ [6]; the same space group is adopted by Ca_2FeSbO_6 and $SrCaFeSbO_6$ at RT [3, 6,26], apparently due to the smaller A-site cation(s). The space group of the hexagonal Ba_2FeSbO_6 is $P6_3/mmc$ [3,26]. By substituting Sr gradually with Ba in the series $(Sr_{1-x}Ba_x)_2FeSbO_6$ the crystal symmetry should ideally change as follows: $I2/m \rightarrow I4/m \rightarrow Fm\text{-}3m \rightarrow P6_3/mmc$. It is thus of interest to see whether the whole crystal symmetry series can actually be reproduced with and without a change in temperature or pressure.

The phase transitions between the perovskite structured phases mentioned previously have been studied extensively. According to the Landau phase transition theory, transition $I2/m \rightarrow I4/m$ is allowed and must be of first order. Also the $I4/m \rightarrow Fm\text{-}3m$ transition is allowed, but must be of second order. These phase transitions are achieved by octahedral tilting and both $I/2m$ and $I/4m$ are subgroups of $Fm\text{-}3m$ [20,29,30].

2. Experimental

A full series of $(Sr_{1-x}Ba_x)_2FeSbO_6$ samples was prepared through sol-gel synthesis to guarantee the same high degree of initial cation mixing and particle size of the product for all the samples. The starting materials, $SrCO_3$ (Aldrich; ≥99.9%, $BaCO_3$ (Merck; >99%) and Sb_2O_3 (Merck; >99%) were dissolved in aqueous citric acid (Sigma-Aldrich; 99%) solution; the citric acid to cation molar ratio was kept at 5:1, but the pH of the solution was not adjusted. Then, Fe_2O_3 (Sigma-Aldrich; ≥99%) was dissolved in oxalic acid (Fluka; 97%) water solution, with the oxalic acid to Fe molar ratio fixed to 5:1 as well. The starting materials were added to the citric acid/water solution in the following order: $SrCO_3$, $BaCO_3$, Sb_2O_3 and Fe-solution. Ethylene glycol (Alfa Aesar; 99%) was added to the combined citric acid plus oxalic acid solution (with cation to ethylene glycol molar ratio of 2:1) after which water was evaporated until no bubble formation was seen. The tiny precipitation (presumably barium oxalate) which formed in some cases after the Fe-oxalic acid solution addition could be eliminated by tuning the amount of water and evaporation rate.

The dried gels were initially heated to 135 °C for 12 hours and then calcined in air first at 650 °C for 12 hours and then at 1150 °C for 12 hours. The calcined and ground (Cole-Parmer 750 W ultrasonic processor) powders were pressed into pellets by cold isostatic pressing (100 MPa water pressure, in waterproof nitrile rubber pouch to prevent contamination from the walls of conventional steel die) and fired in furnace in air twice at 1300 °C for 24 hours with an intermediate grinding. Samples were allowed to cool down to RT relatively slowly with a cooling rate of 200 °C/h in maximum to prevent the possible preservation of the high-temperature crystal structure and/or oxygen non-stoichiometry.

High-pressure samples were prepared from the selected ambient-pressure (AP) samples in a cubic-anvil-type HP synthesis apparatus by pressing at 1000 °C and ca. 4 GPa for 15 minutes. The sample powder was put in a gold capsule which was placed inside a carbon sleeve separated with a boronitride sleeve and end plugs. The carbon sleeve acts as an internal heating element. Finally the sleeved capsule was placed inside a pyrophyllite cube which acts as a pressure transferring media. Molybdenum disks and steel rings were stacked on top of and below of the sleeve and capsule assembly to separate them from the current carrying anvils. The sample amount from a single synthesis batch was 90–100 mg. After the HP heat treatment the sample was first allowed to cool down for ten minutes before the pressure was slowly lowered to the ambient.

X-ray diffraction (XRD; PANalytical X'Pert PRO MPD α-1 powder diffractometer, programmable divergence slits, Johansson-monochromator, Cu Kα-1 radiation) patterns were collected after every synthesis step to follow the phase formation reactions. For the final AP and HP products the crystal structure was refined through Rietveld refinement using the software Fullprof [31]. The expected Sr to Ba ratio in the samples was confirmed with XRF measurements (PANalytical Axios mAX).

Bonding characteristics of the A- and B-site cations were studied through bond valence sum (BVS) calculations [32]. The bond valence value BV for individual bonds was calculated as

$$BV = e^{\frac{R_0 - R}{B}} \quad (3)$$

where R_0 and B are parameters characteristic to the bonding pair, and R is the bond length; the following parameters were used (cation/R_0 (Å)/B (Å)): Sr/2.118/0.37, Ba/2.285/0.37, Fe/1.759/0.37 and Sb/1.904/0.43. The A-site BVSs were calculated as arithmetic sums of the Sr and Ba BVSs. Since our samples exhibited various S values, we also tested a modified BVS model [33] where degree-of-order at the B site is taken into account by taking arithmetic average of the BVSs at each crystallographic site. However, this did not yield satisfactory results in our case. It must also be emphasized that the oxygen positions determined from conventional laboratory XRD data may not be very accurate; this inaccuracy naturally affects the calculated bond lengths and therefore the resultant BVS values. For comparison, we calculated the BVS values for the two end members of the series, Sr_2FeSbO_6 and for Ba_2FeSbO_6, using neutron diffraction data published for these phases [6,34].

Thermogravimetric measurements (TG; Netzsch Jupiter STA 449 C and PerkinElmer Pyris 1 TGA) were carried out to investigate the phase and oxygen-content stabilities of the samples. The measurements were performed in Al_2O_3 crucibles in the temperature range of 30–1500 °C with a heating rate of 10–40 °C/min in air, N_2 and O_2 gas flows of 50 mL/min. Absolute oxygen contents were determined for the samples using two independent methods: thermogravimetric reduction and polarography. The TG reductions were carried out by heating a sample of ca. 10 mg in 5% H_2/Ar gas flow with a heating rate of 40 °C/min up to 1200 °C [35]. For the polarographic determination a sample portion of ca. 100 mg was dissolved in a mixture of 1 mL of hot concentrated HCl and 1 mL of 0.025 M chloroanilic acid (Aldrich) water solution (to complex Sb and thereby keep it in the solution), followed by an immediate cooling down of the solution. Polarographic measurements (Metrohm 797 VA Computrace; standard application number 61 for Fe) were performed in 1 m-% sodium pyrophosphate ($Na_4P_2O_7 \cdot 10\ H_2O$; Sigma) support electrolyte between voltages -50–-1300

mV, using drop mercury electrode as a working electrode, Pt as an auxiliary electrode and Ag/AgCl/KCl (3 mol/L) as a reference electrode. Relative amounts of different iron species are determined by reducing iron in the solution from Fe(III) to Fe(III) and finally to Fe(0).

Room-temperature ^{57}Fe Mössbauer spectra (Topologic Systems Inc. FGX-222ST Mössbauer spectrometer, Cyclotron ^{57}Co/Rh source) were collected for selected AP and HP samples at 4 mm/s. A sample of ca. 40 mg was embedded into a polymer matrix (Pattex 100% glue, Henkel) on an iron free Al foil, forming ca. 2 mm thick and 22 mm diameter disk, giving a sample density of ca. 0.13 mg/mm^3. The spectra were fitted with two Fe(III) components using software Mosswin (version 3.0i); the parameters fitted were: chemical isomer shift relative to α-Fe, relative intensities, quadrupole splitting and resonance line widths.

3. Results and Discussion

Our sol-gel synthesis yielded high-quality samples without impurity phases within the entire substitution range of $(Sr_{1-x}Ba_x)_2FeSbO_6$. According to the XRF measurements, the actual Ba to Sr ratio followed the intended substitution level x in a highly accurate manner. After the final AP calcination at 1300 °C, the sample pellets were dark brown at the Sr end of the series and turned into dark green at the Ba end of the series and finally into mustard yellow in the case of Ba_2FeSbO_6. The HP samples were dark brown as pellets and lighter in colour as a ground powder, that is, yellow to yellow-orange.

From the polarographic and TG-reduction experiments, all the samples were found to be oxygen stoichiometric within the estimated accuracy of the analyses (±0.03 for the oxygen content per formula unit). Also, our TG measurements carried out in both O_2 and N_2 atmospheres confirmed that the phases remain oxygen-stoichiometric upon heating (up to 1200 °C). Since the Mössbauer data confirmed the trivalent state for iron, we may calculate from the sample stoichiometry that antimony in our samples is pentavalent. For the $A_2B'B''O_6$ double-perovskite family, valence mixing between the B' and B'' cations has been observed for several pairs of B-site constituents [23,36–40]. However, it seems that this is not the case in the present system.

For the crystal structures in the $(Sr_{1-x}Ba_x)_2FeSbO_6$ system, we first discuss our AP samples. Rietveld refinement results and profiles for all samples are given in the Supplementary material section. X-ray diffraction patterns (Fig. 1) for the Sr-rich samples of x = 0 and 0.05 were readily indexed and refined in space group *I*2/*m*. An obvious phase change occurs in the range from x = 0.05 to 0.10, where the Bragg reflections with Miller indices 404 and 044 of *I*2/*m* merge into a single 044 reflection of space group *I*4/*m*. By inspecting the XRD pattern for x = 0.075 it is seen that the sample is of the *I*2/*m* phase or a mixture of *I*2/*m* and *I*4/*m*. The x = 0.10 sample was readily refined with the two-phase *I*2/*m* and *I*4/*m* model. Due to strong peak overlapping and correlation, the refined structure parameters and also the phase composition, 45% of *I*2/*m* and 55% of *I*4/*m*, are only indicative. The transition to space group *I*4/*m* is found be essentially complete for x = 0.125.

Between samples x = 0.15 and 0.20, the *I*4/*m* reflections 004 and 220 merge into single 400 reflection of the cubic space group *Fm*-3*m*. We plotted the peak width (FWHM, Supplementary material section, Fig. S37) of the merging 004/220 reflection and 400 reflection against the Ba content x, but no strong change in the trend, neither incline nor decline, could be seen in the plot after x = 0.2. Therefore, merging of the 004 and 220 reflections into the single 400 reflection was complete when the two separate reflections disappeared, indicating that the crystal structure transition from *I*4/*m* to *Fm*-3*m* is reached early in the solid solution series, around x = 0.20. Also the *I*4/*m* reflections at the higher 2θ angles, that is, those of 060, 352, 532, 336 and 028, merge into 660 and 822 reflections of the space group *Fm*-3*m*. A shoulder from the *I*4/*m* reflections can still be seen for the x = 0.15 sample, but not at x = 0.20 anymore. Also this change is abrupt indicating a first order phase transition. For comparison, we note that according to temperature-dependent XRD measurements for Sr_2FeSbO_6 [6], the transition from *I*2/*m* to *I*4/*m* upon increasing temperature proceeds through a mixed region

with both the *I*2/*m* and *I*4/*m* phases coexisting, but the transition from *I*4/*m* to *Fm*-3*m* is continuous without the two-phase coexistence.

Upon increasing the Ba content, the sample x = 0.20 was the first which could be indexed and refined in space group *Fm*-3*m*. From x = 0.20 to 0.825, Rietveld refinement of the XRD patterns yielded nearly identical goodness-of-fit χ^2 values for the two space groups, *I*4/*m* and *Fm*-3*m*; the same conclusion could be made by visual observation of the refined profiles. In the case of *I*4/*m*, the cell parameter a*√2 almost equals the cell parameter c [c/(a*√2) ≈ 1.0] meaning that the unit cell distortion, i.e. the degree-of-tetragonality, is minimal. The c/a (c/a*√2) ratio is plotted in the Supplementary material section, Fig. S38.

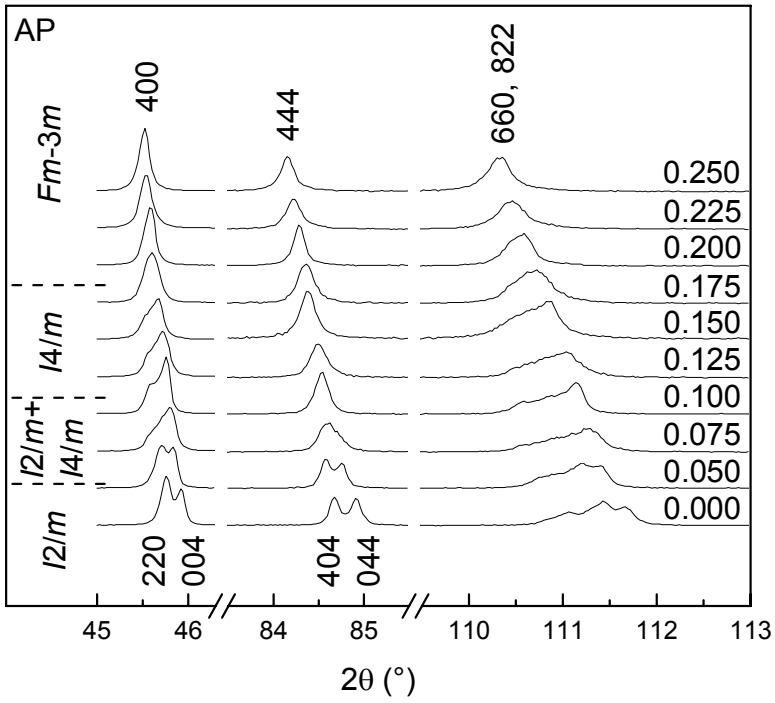

Fig. 1. XRD patterns for our AP $(Sr_{1-x}Ba_x)_2FeSbO_6$ samples in the Sr-rich range of x = 0–0.25, showing the merging of the 404 and 044 reflections of space group *I*2/*m* and 220 and 004 of space group *I*4/*m* with increasing Ba content x.

The aforementioned behaviours can also be seen in the plots of cell parameters against the Ba content x (Fig. 2). The *I*2/*m* to *I*4/*m* transition should be seen in the a and b cell parameters since tilting of the BO_6 octahedra typical to *I*2/*m* should vanish when the space group *I*4/*m* is reached and a equals b. Another anomaly should be seen when the transition from *I*4/*m* to *Fm*-3*m* occurs since the octahedral tilting in the a-b plane should disappear. From Fig. 2, changes in the slope and anomalies in parameter c against the Ba content can be seen in three areas, around x ≈ 0.10, 0.20 and 0.85. It is also seen that the slope for the *Fm*-3*m* cell parameters is different in the single (x = 0.20–0.80) and dual (x = 0.85–0.95) phase regions; assuming that the Vegard's law applies it seems that the Ba content of the cubic phase does not increase strongly in the two-phase region anymore. We should mention here that the B-site cation ordering and anti-phase (out-of-phase) tilting may give rise to the same superlattice reflections. There are a few possible space groups in which the B-site ordered double perovskites can crystallise with in-phase octahedral tilting and which at the same time share the correct group-subgroup relationships relevant to this study, for example *P*4/*mnc*, $P2_1/n$ and *C*2/*c* [4,29,30]. However, these reflections were not seen in our XRD patterns.

The transition from *Fm*-3*m* to *P*6$_3$/*mmc* is seen more clearly since the Bragg reflections from the hexagonal phase appear between x = 0.80 and 0.85, and the two phases co-exist up to x = 0.95 where the single hexagonal phase is reached (Fig. 3). Crystallographically this is first order transition and the fraction of the hexagonal phase increases gradually. The complete AP phase diagram for the $(Sr_{1-x}Ba_x)_2FeSbO_6$ system is sketched in Fig. 2.

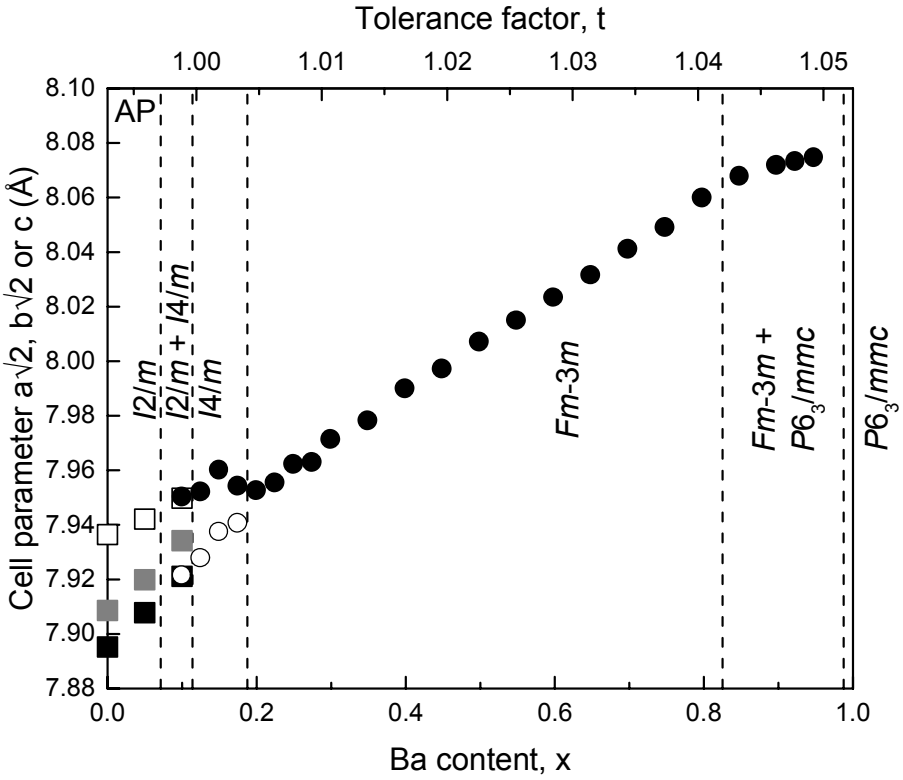

Fig. 2. Phase diagram and cell parameters a√2 (white squares for *I*2/*m* and white circles for *I*4/*m*), b√2 (grey squares for *I*2/*m*) and c (black circles) plotted against the Ba content x for our AP $(Sr_{1-x}Ba_x)_2FeSbO_6$ samples. For the single and dual phase *Fm*-3*m* regions only the cell parameter c is given.

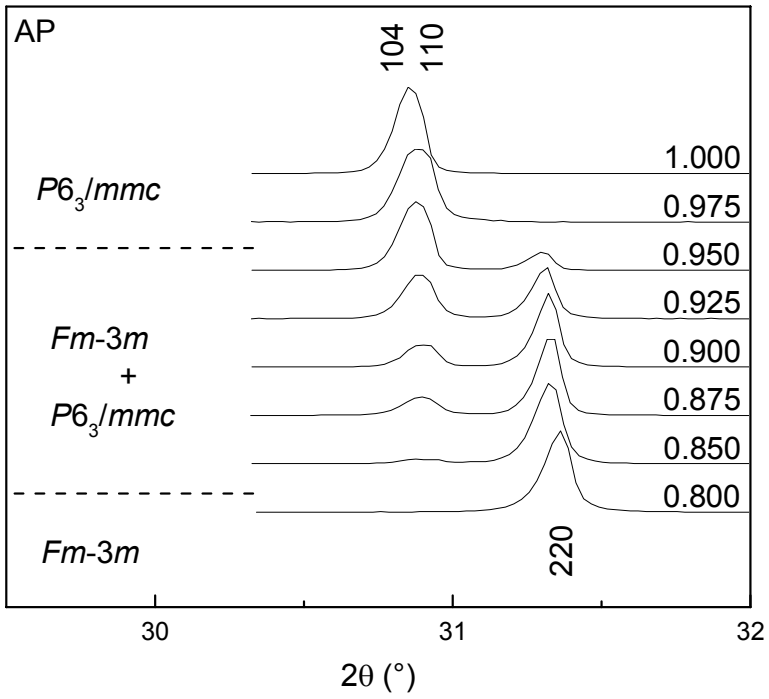

Fig. 3. XRD patterns for our AP $(Sr_{1-x}Ba_x)_2FeSbO_6$ samples in the Ba-rich range of x = 0.80–1, showing a continuous transition from the cubic to the hexagonal structure with increasing Ba content x.

When the structure is considered purely from the tolerance parameter point of view, the ideal t = 1.00 condition is reached when x ≈ 0.12. Experimentally the cubic perovskite is obtained under ambient pressure from x ≈ 0.20 to 0.80. This interval corresponds to the t values from 1.00 to 1.04. The co-existence of cubic and hexagonal phases between x ≈ 0.80 and 0.975 corresponds to t values from 1.04 to 1.05. It is understood that the concept of the tolerance parameter gives good guidelines, but the simple geometrical analysis is not enough to fully explain the reasons for the phase formation. It is also recognized that the assumptions made using only ionic radii from the literature might not be true for all perovskites, as demonstrated in previous literature as well [4]. As the unit cell expands, naturally the bond lengths increase. For the AP phases, the average Fe-O, Sb-O and Sr/Ba-O bond lengths (Fig. 4) increase in similar fashions as the cell parameters. As calculated from the tabulated values by Shannon, the following bond lengths would be expected: Fe-O 2.05 Å, Sb-O 2.00 Å, Sr-O 2.84 Å and Ba-O 3.01 Å. Finally we like to mention that, since both the increasing temperature and the larger-for-smaller cation substitution lead to cell expansion, we found it interesting to plot (the plots not shown here) the linear portions of the cell parameters against both the Ba content and the temperature (from literature data [6]). The cell parameter a of the *Fm*-3*m* phase in the single phase region changes with the slope 0.176 Å per x for our $(Sr_{1-x}Ba_x)_2FeSbO_6$; this corresponds to ca. $0.17*10^{-3}$ Å per °C for Sr_2FeSbO_6.

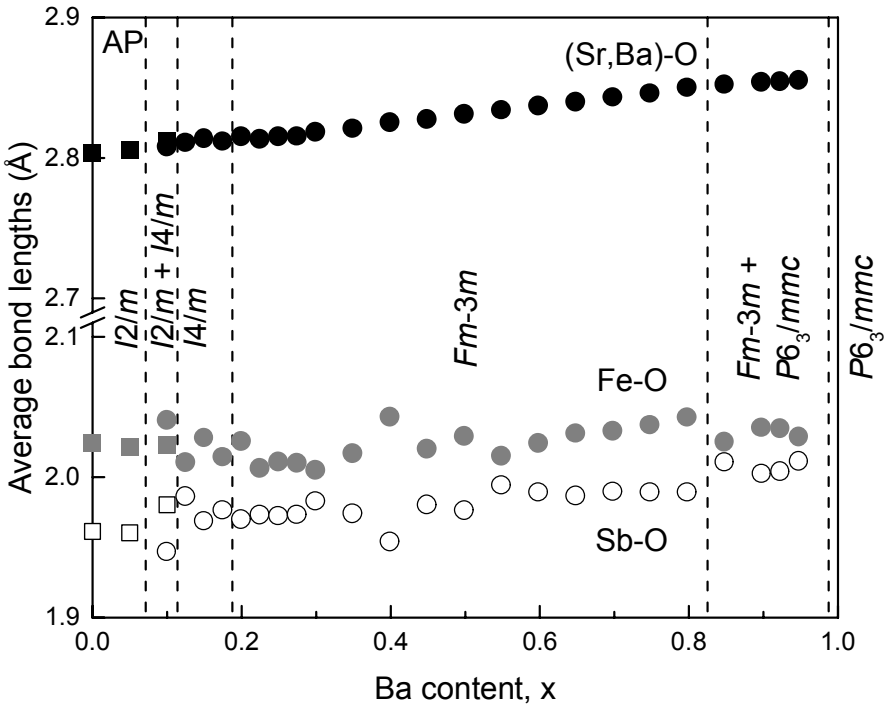

Fig. 4. Average (Sr,Ba)-O (black squares *I*2/*m* and black circles *I*4/*m* and F*m*-3*m*), Fe-O (grey squares *I*2/*m* and grey circles *I*4/*m* and F*m*-3*m*) and Sb-O (white circles *I*2/*m* and white circles *I*4/*m* and F*m*-3*m*) bond lengths plotted against the Ba content x for the cubic and pseudocubic phases in our AP $(Sr_{1-x}Ba_x)_2FeSbO_6$ samples.

The degree-of-order parameter for the B-site cations was calculated from the Rietveld refinement results. From Fig. 5, the value of S is the highest (ca. 90%) at the Sr-rich end of the series, decreasing with increasing Ba content first moderately and then more strongly after $x \approx 0.70$. dropping down to ca. 65% in the dual phase area. In the hexagonal x = 1 end phase, the degree-of-order is significantly low, that is, less than 10%. Interestingly, the trend seen here for the $(Sr_{1-x}Ba_x)_2FeSbO_6$ system is very similar to previous observations for related double perovskite systems for which the increase in the A-site cation radius has been found to lead to a decrease in S [24,38,41]; the reasons behind this trend are not fully explained, though, and may naturally be different in the different systems. We also calculated similar degree-of-order parameters based on our Mössbauer spectroscopy data (also plotted in Fig. 5 for comparison): a very similar declining trend with increasing x was found even though the absolute values are systematically somewhat lower. Here it should be noted that the degree-of-order value (as calculated from Eq. 2) "overemphasizes" the deviation in the results of the two techniques in comparison to the actual fractional occupancies of Fe and Sb at the two B-cation sites. For example, for the x = 0 sample the fractional Fe site occupancies are ~0.95 (Rietveld) and ~0.8 (Mössbauer), while the values calculated for the degree-of-order parameter are ~0.9 (Rietveld) and ~0.6 (Mössbauer). Moreover, since octahedral tilting and B-site cation ordering affect the same superlattice reflections in XRD patterns, a systematic error in the site occupancies is likely because the amount of tilting depends on the oxygen positions, which in turn are not accurately determined by XRD.

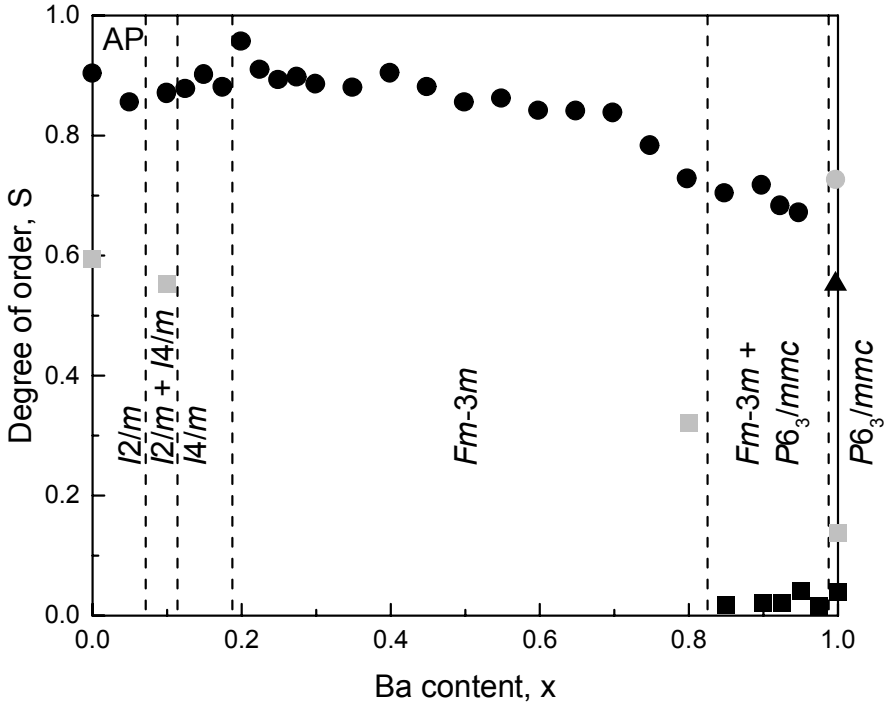

Fig. 5. Degree-of-order plotted against the Ba content x for our AP cubic or pseudocubic (black circles), hexagonal (black squares) and x = 1 HP (black triangle) $(Sr_{1-x}Ba_x)_2FeSbO_6$ samples from Rietveld refinement results and for AP (grey squares) and x = 1 HP (grey circle) from Mössbauer spectra fittings.

Then we discuss the effects of the HP heat treatment. The phase diagram and cell parameters for our HP samples are displayed in Figure 6. Among the samples treated a phase transformation was seen for the sample x = 0.10 from dual phase *I*2/*m* and *I*4/*m* to single phase *I*4/*m* and for all samples containing the hexagonal non-perovskite *P*6$_3$/*mmc* phase which transformed to the cubic *Fm*-3*m* perovskite structure. We also investigated the thermal stabilities of our HP treated samples. Quite interestingly, the metastable cubic structure of the x = 1 HP sample remained thermally stable upon heating in 1 atm air flow up to the temperature as high as ca. 1100 ºC; only above this temperature the structure transformed back to the hexagonal structure.

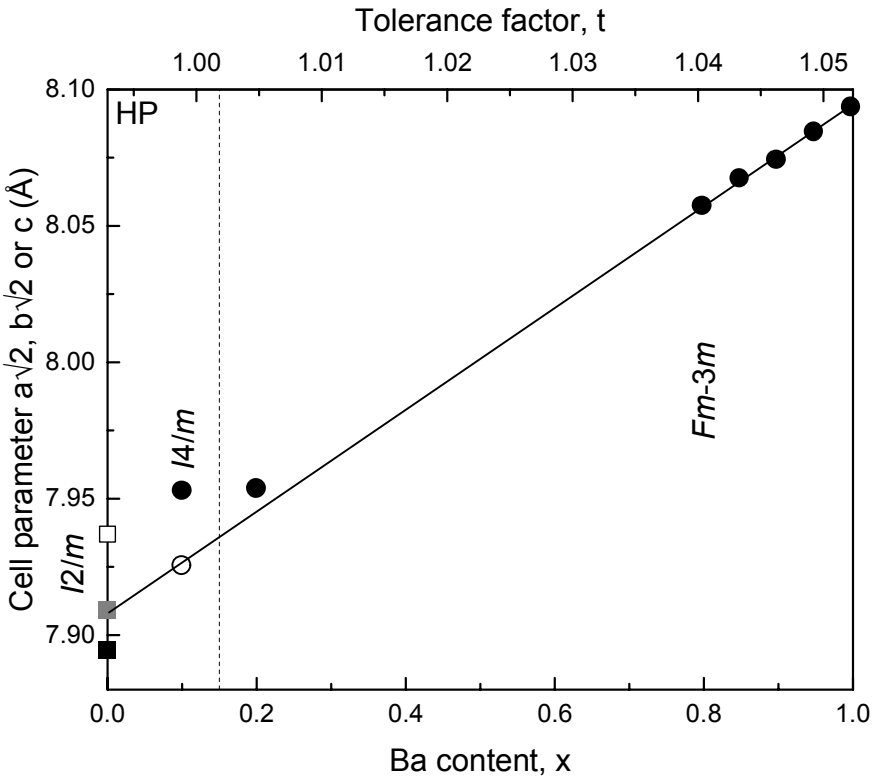

Figure 6. Phase diagram and cell parameters a√2 (white square for *I*2/*m* and white circle for *I*4/*m*), b√2 (grey square for for *I*2/*m*) and c (black square for *I*2/*m* and black circles for *I*4/*m* and *Fm*-3*m*) against Ba content x for the HP samples. For the *Fm*-3*m* region only the cell parameter c is given. The black diagonal line is only a guide to the eye. No phase boundary lines are drawn at the *I*2/*m* and *I*4/*m* region.

An interesting observation can be made from Fig. 7 where we plot the bond length differences between the hexagonal AP and cubic HP phases: the Fe-O (B-O), Sb-O (B'-O) and two different (Sr,Ba)-O (A1-O is Wyckoff position *2a*, A2-O is Wyckoff position *4f*) bond lengths are compared to those in the cubic HP samples. From Fig. 7, the (Sr,Ba)-O bond lengths decrease upon the HP treatment whereas the general trend for the Fe-O and Sb-O bonds is just the opposite, but smaller. The large bond length increase for the Fe-O bond in the x = 0.85 sample is most likely due to an inaccuracy in the oxygen position refinement.

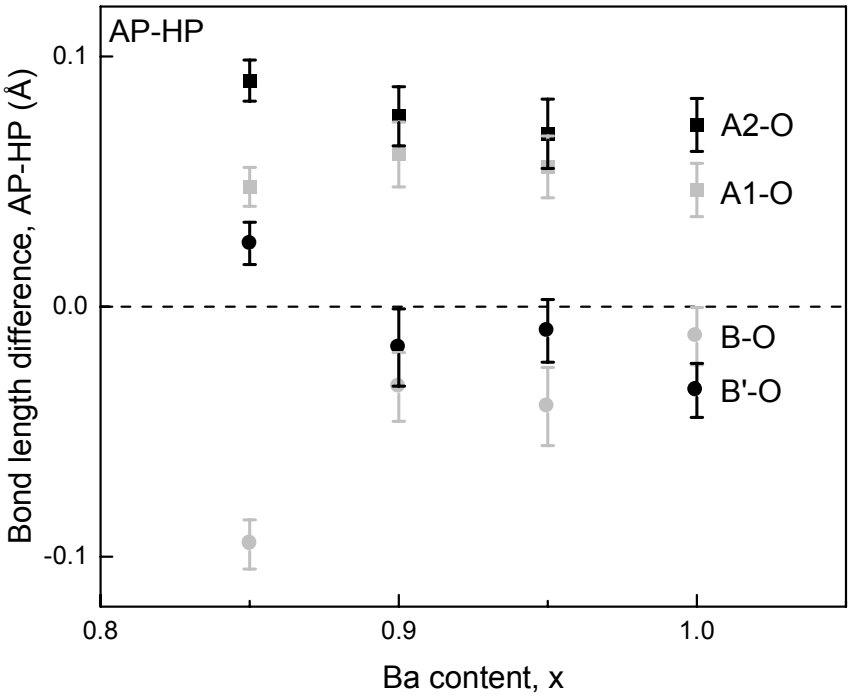

Fig. 7. Average bond length differences (including confidence interval at the 1-sigma level) for the hexagonal AP and cubic HP samples; Fe-O (B-O) (grey circles), Sb-O (B'-O) (black circles), A1-O (grey squares) and A2-O (black squares).

The BVS calculation results are summarized in Fig. 8. For the B-site cations the BVS values are reasonable over the whole substitution range x. For comparison we calculated BVSs based on the neutron diffraction data by Faik et al. [6] for the two end members; the results were in an excellent agreement with our XRD based results. From Fig. 8, the general trend for the B-site cations is that the BVSs are slightly declining towards the Ba-rich end of the series, and contrarily, the A-site BVSs are increasing.

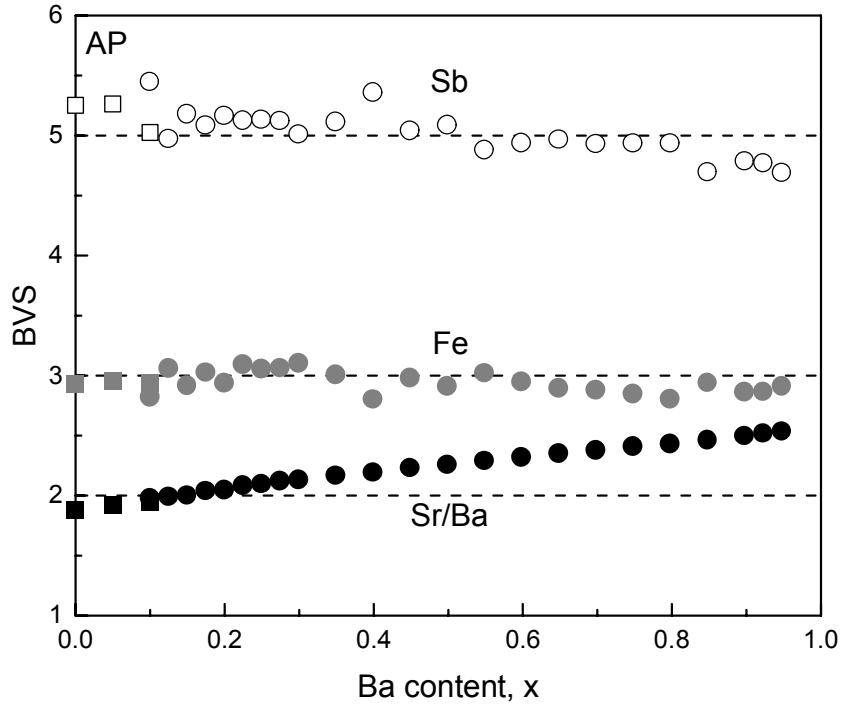

Fig. 8. BVSs calculated for Sr/Ba (black squares for *I*2/*m* and black circles for *I*4/*m* and *Fm*-3*m*), Fe (grey squares for *I*2/*m* and grey circles for *I*4/*m* and *Fm*-3*m* circles) and Sb (white squares for *I*2/*m* and white circles for *I*4/*m* and *Fm*-3*m*) in the $(Sr_{1-x}Ba_x)FeSbO_6$ system as a function of Ba content x. When x = 0.80–0.95, the BVS only for the cubic phase is plotted.

Finally we display in Fig. 9 ^{57}Fe Mössbauer spectra for representative samples. The data confirm the trivalent state of iron in all the samples (isomer shift values between 0.3–0.5 mm/s, as typical for trivalent high-spin iron in oxides [42]). The spectra could be readily fitted with two quadrupole components, corresponding to iron atoms at two different crystallographic sites.

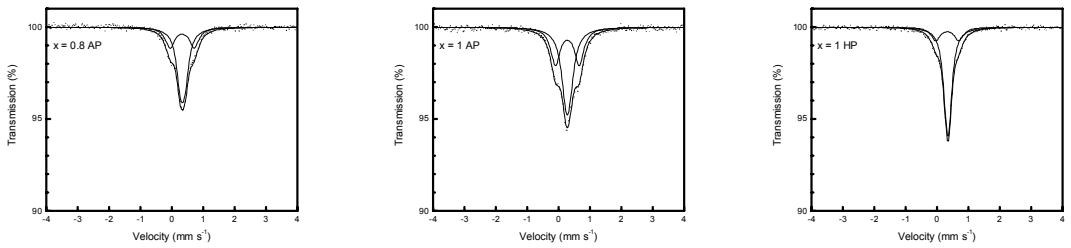

Fig. 9. Mössbauer spectra for AP x = 0.8 (*Fm*-3*m*), AP x = 1 (*P*6$_3$/*mmc*) and HP x = 1 (*Fm*-3*m*).

4. Conclusions

We employed the $(Sr_{1-x}Ba_x)_2FeSbO_6$ series as a flexible model system to systematically investigate the effects of (i) chemical pressure through isovalent A-site cation substitution and (ii) physical pressure through a high-pressure heat treatment, on the cation ordering and crystal symmetry in B-site ordered double perovskites. We synthesized an extensive sample series of Ba-for-Sr substituted samples through sol-gel synthesis. From chemical and XRD analyses all the samples were

confirmed to follow the intended Ba:Sr ratio x, and be oxygen stoichiometric and free from impurity phases within the entire substitution range from x = 0 to 1.

From the structural analysis we were able to demonstrate that chemical pressure and physical pressure work towards the same direction in the $(Sr_{1-x}Ba_x)_2FeSbO_6$ system, and towards a direction opposite to that seen with increasing temperature. Upon increasing the Ba content x, i.e. by gradually releasing the chemical pressure, a gradual structural transformation was realized from the monoclinic *I*2/*m* to tetragonal *I*4/*m*, cubic *Fm*-3*m* and hexagonal $P6_3/mmc$ structure. This is the same transformation sequence previously observed up to *Fm*-3*m* upon heating the parent Sr_2FeSbO_6 phase to high temperatures. Compared to the temperature-induced phase transitions, the effects due to the chemical pressure were found sharper, except in the cubic-hexagonal dual phase region. High-pressure treatment then transformed the hexagonal $P6_3/mmc$ structure of Ba_2FeSbO_6 back to the cubic *Fm*-3*m* structure seen for the ambient-pressure synthesized samples in the range of ca. x = 0.85–1.

From the BVS and bond length calculations we concluded that especially the A-site bond lengths are shorter than expected in the Ba-rich region. Since the B-O bond lengths do not vary as much as the A-O bond lengths at the Ba end of the substitution series, the greatest discrepancy between the ideal tolerance factor and cubic structure arises from the A-O bond. Therefore, the actual tolerance factor might be closer to the ideal unity, as indicated by the phase diagram.

High-pressure heat treatment was employed to stabilize the metastable cubic perovskite structure for the heavier-side end member of the series, i.e. Ba_2FeSbO_6, for the first time. This result was naturally expected, since the cubic phase is the densest and with least structural distortions. The HP treatment causes A-O bonds to compress and that way allow the transformation from the hexagonal to the cubic perovskite structure. Very interestingly, we found the metastable HP phase to be amazingly stable under ambient pressure; upon heating the phase in air the perovskite structure persisted up to ca. 1100 ^{o}C. This high thermal stability of the HP phases allows e.g. the sample powders to be sintered which is a highly useful aspect, having the eyes on e.g. physical property characterization of these metastable phases.

We also investigated the effects of the A-site chemical pressure on the degree-of-order among the B-site cation species. With increasing Ba-for-Sr substitution level, the degree-of-order between Fe and Sb was found to decrease. For the determination of the degree-of-order parameter S we employed both XRD-based Rietveld refinement and ^{57}Fe Mössbauer spectroscopy data. The two techniques revealed highly parallel trends though somewhat different absolute values for S.

References

[1] V.M. Goldschmidt, Naturwissenschaften 14 (1926) 477–485.

[2] R. D. Shannon, Acta Cryst. A 32 (1976) 751–767.

[3] G. Blasse, J. Inorg. Nucl. Chem. 27 (1965) 993–1003.

[4] S. Vasala. M. Karppinen, Prog. Solid St. Chem. 43 (2015) 1–36.

[5] R.S. Roth, J. Res. Nat. Bur. Stand. 58 (1957) 75–88.

[6] A. Faik, J.M. Igartua, E. Iturbe-Zabalo, G.J. Cuello, J. Mol. Struct. 963 (2010) 145–152.

[7] A. Roushown, Y. Masamoto, J. Solid State Chem. 178 (2005) 2867–2872.

[8] B. J. Kennedy, C. J. Howard, B. C. Chakoumakos, J. Phys. Cond. Mat. 11 (1999) 1479–1488.

[9] J. Liebertz, C. J. M. Rooymans, Z. Phys. Chem. Neue Fol. 44 (1965) 242–249.

[10] K. Kohn, R. Fukuda, S. Iida, J. Phys. Soc. Jpn. 22 (1967) 333.

[11] H. Yamauchi, M. Karppinen, Supercond. Sci. Technol. 13 (2000) R33–R52.

[12] T. Aoba, T. Tiittanen, H. Suematsu, M. Karppinen, J. Solid State Chem. 233 (2016) 492–496.

[13] K.-I. Kobayashi, T. Kimura, H. Sawada, K. Terakura, Y. Tokura, Nature 395 (1998) 677–680.

[14] Y.-H. Huang, R. I. Dass, J. C. Denyszyn, J. B. Goodenough, J. Electrochem. Soc. 153 (2006) A1266–A1272.

[15] Y.-H. Huang, R. I. Dass, Z.-L. Xing, J. B. Goodenough, Science 312 (2006) 254–257.

[16] R. H. Mitchell, Perovskites: modern and ancient, Vol. 3, Almaz Press, Thunder Bay, 2002.

[17] J. Lindén, M. Karppinen, T. Shimada, Y. Yasukawa, H. Yamauchi, *Phys. Rev. B* 68 (2003) 174415-1–174415-5.

[18] K. I. Kugel', D. I. Khomskiĭ, Sov. Phys. Usp. 25 (1982) 231–256.

[19] M. T. Anderson, K. B. Greenwood, G. A. Taylor, K. R. Poeppelmeier, Prog. Solid St. Chem. 22 (1993) 197–233.

[20] C. J. Howard, B. J. Kennedy, P. M. Woodward, Acta Cryst. B 59 (2003) 463–471.

[21] M. W. Lufaso, P. M. Woodward, Acta Cryst. B 60 (2004) 10–20.

[22] G. King, P. M. Woodward, Cation ordering in perovskites, J. Mater. Chem. 20 (2010) 5785–5796.

[23] P. Woodward, R.-D. Hoffmann, A.W. Sleight, J. Mater. Res. 9 (1994) 2118–2127.

[24] T. Shimada, J. Nakamura, T. Motohashi, H. Yamauchi, M. Karppinen, Chem. Mater. 15 (2003) 4494–4497.

[25] Y. Yasukawa, J. Lindén, T.-S. Chan, R.-S. Liu, H. Yamauchi, M. Karppinen., J. Solid State Chem. 177 (2004) 2655–2662.

[26] P. D. Battle, T. C. Gibb, A. J. Herod, S.-H. Kim, P. H. Munns, J. Mater. Chem. 5 (1995) 865–870.

[27] M. Li, H.-M. Yuan, W. Xu, M. Han, L.-R. Yao, M. Yang, S.-H. Feng, Chem. Res. Chinese Universities 28 (2012) 788–791.

[28] N. Hayashi, T. Yamamoto, H. Kageyama, M. Nishi, Y. Watanabe, T. Kawakami, Y. Matsushita, A. Fujimori, M. Takano, Angew. Chem. 123 (2011) 12755–12758.

[29] M. Gateshki, J. M. Igartua, E. Hernández-Bocanegra, J. Phys. Cond. Mat. 15 (2003) 6119–6217.

[30] C. J. Howard, H. T. Stokes, Acta Cryst. A 61 (2005) 93–111.

[31] J. Rodriguez-Carvajal, Physica B 192 (1993) 55–69.

[32] I. D. Brown, Chem. Soc. Rev. 7 (1978) 359–376.

[33] F. Bosi, Acta Cryst. B70 (2014) 864–870.

[34] M. Retuerto, J. A. Alonso, M. J. Martínez-Lope, M. García-Hernández, K. Krezhov, I. Spirov, T. Ruskov, M. T. Fernández-Díaz, Eur. J. Inorg. Chem. 2008 (2008) 2286–2294.

[35] M. Karppinen, L. Niinistö, H. Yamauchi, J. Therm. Anal. 48 (1997) 1123–1141.

[36] T. Yamamoto, J. Liimatainen, J. Lindén, M. Karppinen, H. Yamauchi, J. Mater. Chem. 10 (2000) 2342–2345.

[37] Y. Matsuda, M. Karppinen, Y. Yamazaki, H. Yamauchi, J. Solid State Chem. 182 (2009) 1713–1716.

[38] Y.H. Huang, M. Karppinen, H. Yamauchi, J B. Goodenough, Phys. Rev. B 73 (2006) 104408-1–104408-5.

[39] S. Vasala, M. Lehtimäki, Y.H. Huang, H. Yamauchi, J.B. Goodenough, M. Karppinen, Chem. Mater. 183 (2010) 1007–1012.

[40] J. Lindén, T. Yamamoto, J. Nakamura, M. Karppinen, H. Yamauchi, Appl. Phys. Lett. 78 (2001) 2736–2738.

[41] Y.H. Huang, J. Lindén, H. Yamauchi, M. Karppinen, Chem. Mater. 16 (2004) 4337–4342.

[42] G.J. Long, Mössbauer Spectroscopy Applied to Inorganic Chemistry. Volume 1, Plenum press, New York, 1984.

Graphical abstract